Electronic Supplementary Information for

Ordered assembly of hybrid room-temperature-phosphorescence thin films showing polarized emission and sensoring for VOCs

Rui Gao,[a] and Dongpeng Yan[ab]*

a: State Key Laboratory of Chemical Resource Engineering, Beijing University of Chemical Technology, Beijing 100029, P. R. China;

b: Beijing Key Laboratory of Energy Conversion and Storage Materials, College of Chemistry, Beijing Normal University, Beijing 100875, P. R. China. E-mail: yandp@bnu.edu.cn, yandongpeng001@163.com

Content:

Preparation of TA/Zn_2Al-LDHs: TA/Zn_2Al-LDHs material was synthesized by a co-precipitation method. In brief, solution A: $Zn(NO_3)_2 \cdot 6H_2O$ (0.05 mol) and $Al(NO_3)_3 \cdot 9H_2O$ (0.025 mol). Solution B: NaOH (0.15 mol) and TA (0.015 mol) dissolved in 100 mL of deionized water. Solution A (100 mL) was added dropwise to solution B (100 mL) with vigorous agitation under a nitrogen flow. The pH value at the end of addition was adjusted to 6.6 by further addition of 1.2 mol/L NaOH solution. The reaction mixture was subsequently heated at 60 °C for 12 h. The product was washed with hot, distilled water and anhydrous ethanol thoroughly and then dried in vacuum at 60 °C for 24 h.

Structural and morphology characterization: Powder XRD patterns of all compounds were collected on a Rigaku Ultima-IV automated diffraction system with Cu Kα radiation (λ = 1.5406 Å). Measurements were made in a 2θ range of 3−70° at room temperature with a step of 0.02° (2θ) and a counting time of 0.2 s/step. The operating power was 40 kV, 50 mA. The morphology of the samples was investigated by using a scanning electron microscope (SEM Hitachi S-3500) equipped with an EDX attachment (EDX Oxford Instruments Isis 300), with an acceleration voltage of 20 kV.

The thickness of the sample was obtained by using atomic force microscopy (AFM) software (Digital Instruments, Version 6.12). TEM images were recorded with Philips Tecnai 20 and JEOL JEM- 2010 high-resolution transmission electron microscopes. The accelerating voltage was 200 KV in each case. The Fourier transform infrared (FT-IR) spectra were recorded using a Vector 22 (Bruker) spectrophotometer using the KBr pellet technique in the range 4000-400 cm^{-1} with 2 cm^{-1}resolution.

Optical properties: Photoluminescence (fluorescence and phosphorescence) spectra, the time-resolved luminescence decay spectra and polarized phosphorescence spectra of the samples were performed on an Edinburgh FLS980 fluorescence spectrometer. The UV–vis absorption spectra and UV–vis transmittance spectra were collected on a Shimadzu U-3000 spectrophotometer, with the slit width of 1.0 nm. Phosphorescence quantum yield values at room temperature were estimated using a Teflon-lined integrating sphere (F-M101, Edinburgh) in FLS980 fluorescence spectrometer.

Figure S1. (a) The XRD patterns of TA/LDHs. (b) Photoluminescence (PL) spectra of TA/LDHs. (Excitation wavelength: 320 nm) (c) Photographs of TA/LDHs taken at different time intervals before and after turning-off the excitation. (d) Time-resolved emission decay curve of 350 nm and 490 nm emission from the TA/LDHs.

Figure S2. (a) SEM and (b) TEM images of the TA/LDHs. (c) AFM and the (d) height curves for TA/LDHs.

Figure S3. The energy levels of states for (a) TA and (b) TA/LDHs, respectively.

Figure S4. Polarized phosphorescence profiles and anisotropic value (*r*) for the$(TA/LDHs@PAA)_n$. (a) $n = 20$, (b) $n = 40$, (c) $n = 60$, (d) $n = 80$.

Figure S5. The phosphorescent response profiles of the $(TA/LDHs@PAA)_{80}$ TF to different VOCs.

Figure S6. The fluorescent response profiles of the $(TA/LDHs@PAA)_{80}$ TF to (a) nitrobenzene and (b) pyridine with different concentrations.

Figure S7. FT-IR spectra of the TA/LDHs@PAA before and after treated with (a) pyridine (b) nitrobenzene.

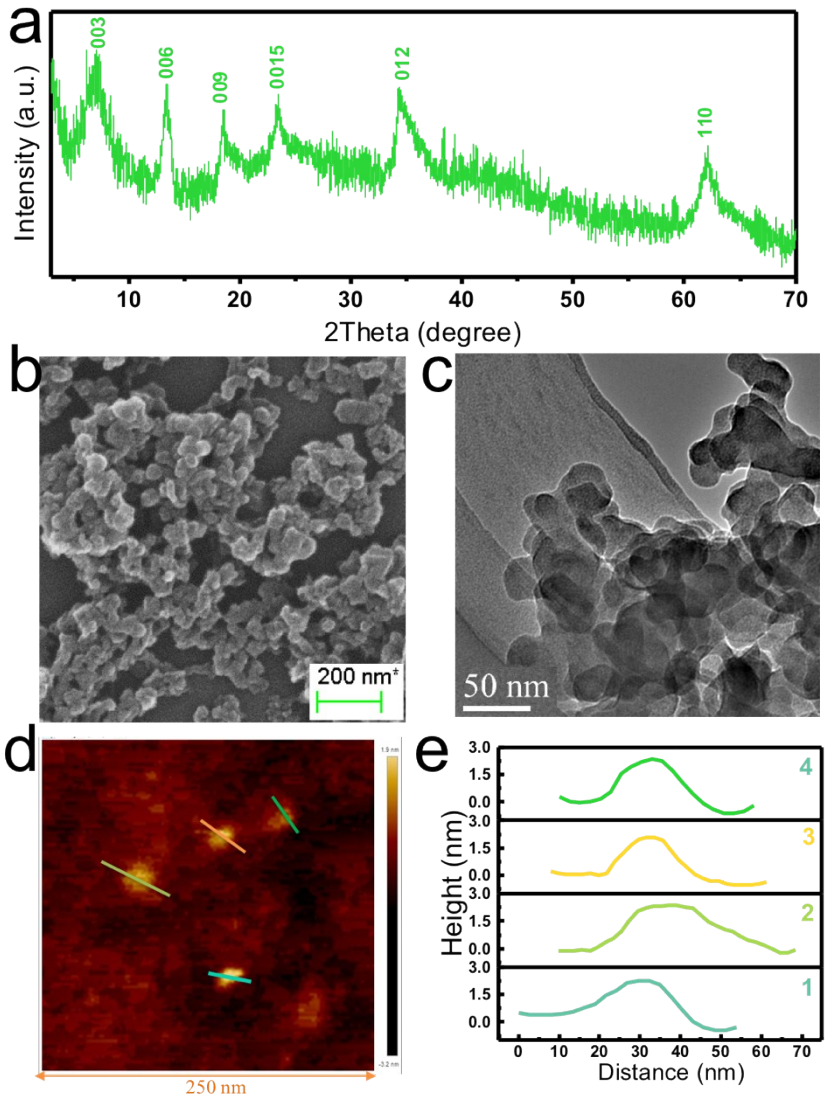

Figure S1. (a) The XRD patterns, (b) SEM and (c) TEM images of the TA/LDHs. (d) AFM and the (e) height curves for TA/LDHs.

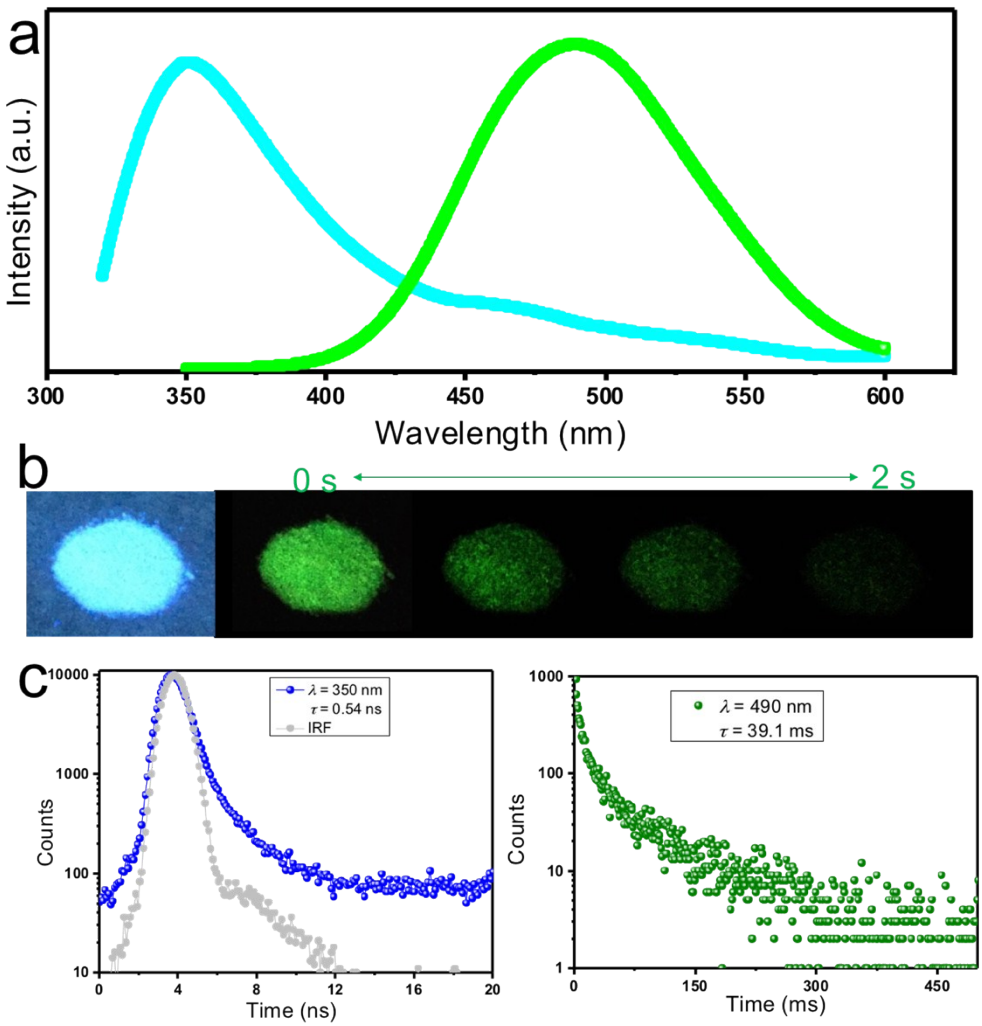

Figure S2. (a) Photoluminescence (PL) spectra of TA/LDHs. (Excitation wavelength: 320 nm) (b) Photographs of TA/LDHs taken at different time intervals before and after turning-off the excitation. (c) Time-resolved emission decay curve of 350 nm and 490 nm emission from the TA/LDHs.

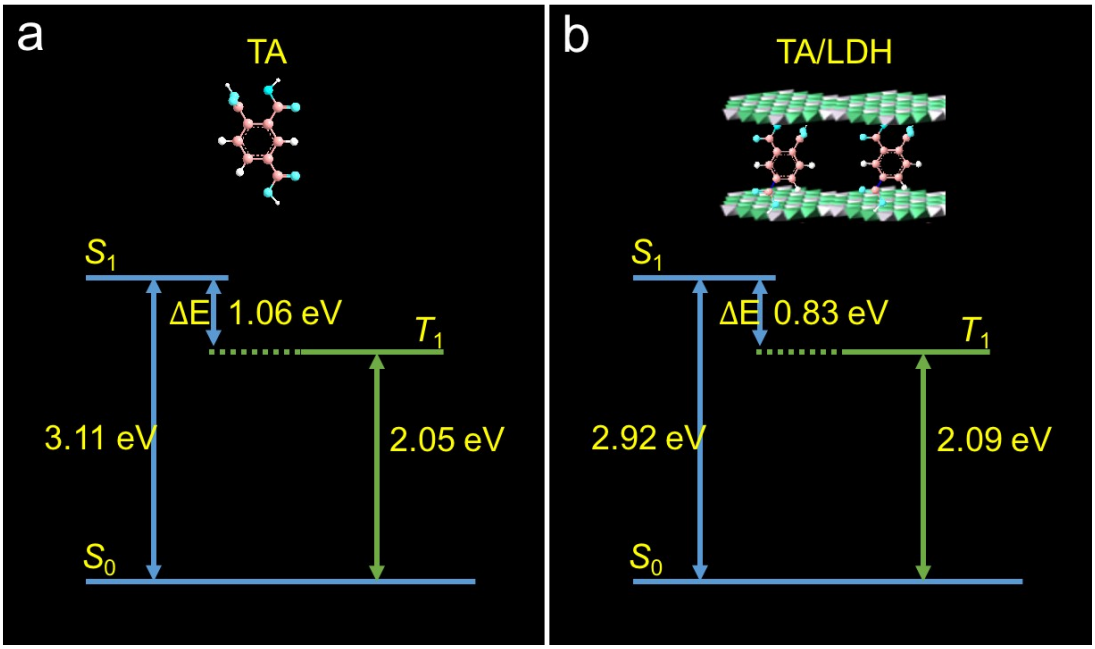

Figure S3. The energy levels of states for (a) TA and (b) TA/LDHs, respectively.

In theory, the possibility of transition between two states (S → T) is connected with the oscillator strength (*f*), which is typically less than 1. The transition between two states can be regarded as prohibition when oscillator strength is less than 0.01. Typically, the room-temperature phosphorescence (RTP) process can be evaluated by electric transition dipole moment of $T_1 \rightarrow S_0$ as defined below (such as *J. Chem. Theory Comput,*. 2013, **9**, 1132):

$$\mu_{T_1 \rightarrow S_0} \propto \sum_n \frac{\xi(T_1, S_n)\mu_{S_n \rightarrow S_0}}{\Delta E_{T_1 \rightarrow S_n}}$$

In this formula, ξ (T_1, S_n) is the spin−orbit coupling (SOC) between the singlet S_n and lowest triplet T_1 states, $\mu_{S_n \rightarrow S_0}$ is the electric transition dipole moment between the intermediate S_n singlet and ground states, and $\Delta E_{T_1 \rightarrow S_n}$ is the energy difference between T_1 and S_n. Therefore, the high-efficiency RTP should meet the standards of large spin−orbit coupling and low $\Delta E_{T_1 \rightarrow S_n}$.

The aromatic carboxylic acid systems with RTP performances have been detected in the previous work from both experimental and theoretical studies. For example, Yuan et al (*Chem. Sci.*, 2015, 6, 4438) have shown that the solid-state phthalic acid

analogues present RTP since the $n \rightarrow \pi^*$ transition of the carboxylic group is favorable for the enhancement of intersystem crossing from singlet to triplet states. Shuai *et al* (*J. Phys. Chem. Lett.,* 2016, **7**, 2893) have studied RTP photophysical process of terephthalic acid and isophthalic acid using a combined quantum and molecular mechanics (QM/MM) method. They found that the electrostatic interaction plays an important role in increasing transition dipole moment and radiative pathway $T_1 \rightarrow S_0$. The nonradiative decay process is also blocked by restriction of the high-frequency C=O stretching vibration.

In this work, the molecular structure of trimellitic acid (TA) belongs to aromatic carboxylic acids. The fluorescence located at ca. 350 nm can be attributed to the $\pi \rightarrow \pi^*$ transition in the conjugated benzene; the RTP process is similar to those of as-reported terephthalic acid and isophthalic acid. Furthermore, after fixed into 2D nanogallery of the positive-charged LDH layers, the geometric confinement effect and electrostatic interaction between the host layer and the TA guest can further enhance the spin-orbit coupling $\xi(T_1, S_1)$, and stabilize the long-lived triplet excited states. As shown in Figure S3, the $\Delta E_{T_1 \rightarrow S_1}$ has been further reduced relative to the pristine TP, suggesting that the oscillator intensity of $T_1 \rightarrow S_0$ is increased.

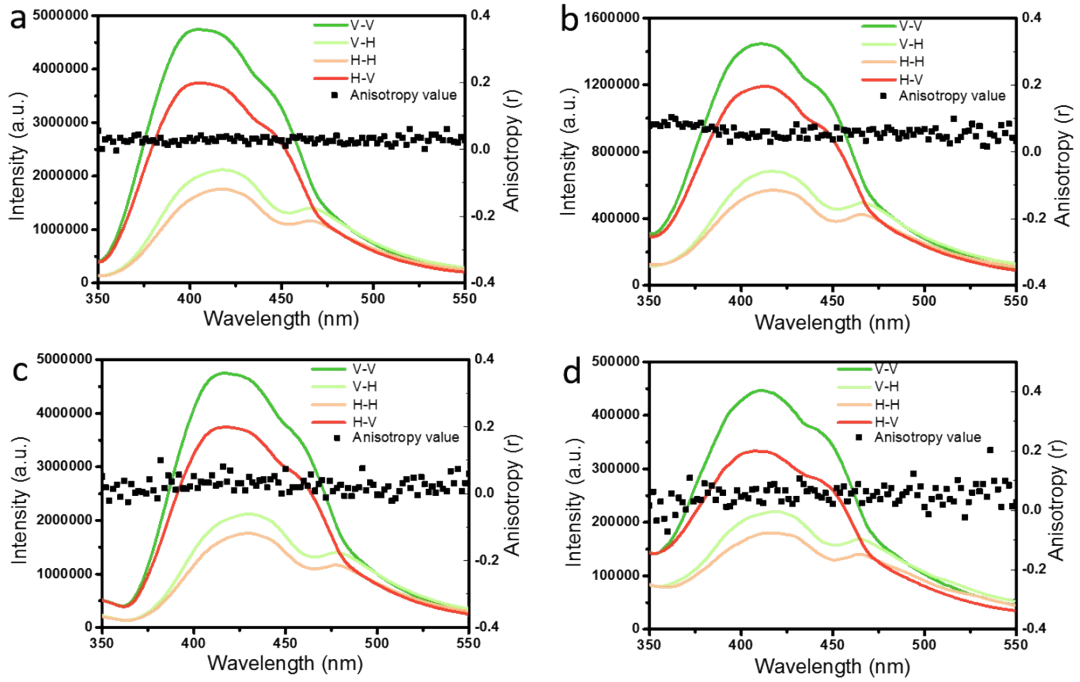

Figure S4. Polarized phosphorescence profiles and anisotropic value (r) for the (TA/LDHs@PAA)$_n$. (a) n = 20, (b) n = 40, (c) n = 60, (d) n = 80.

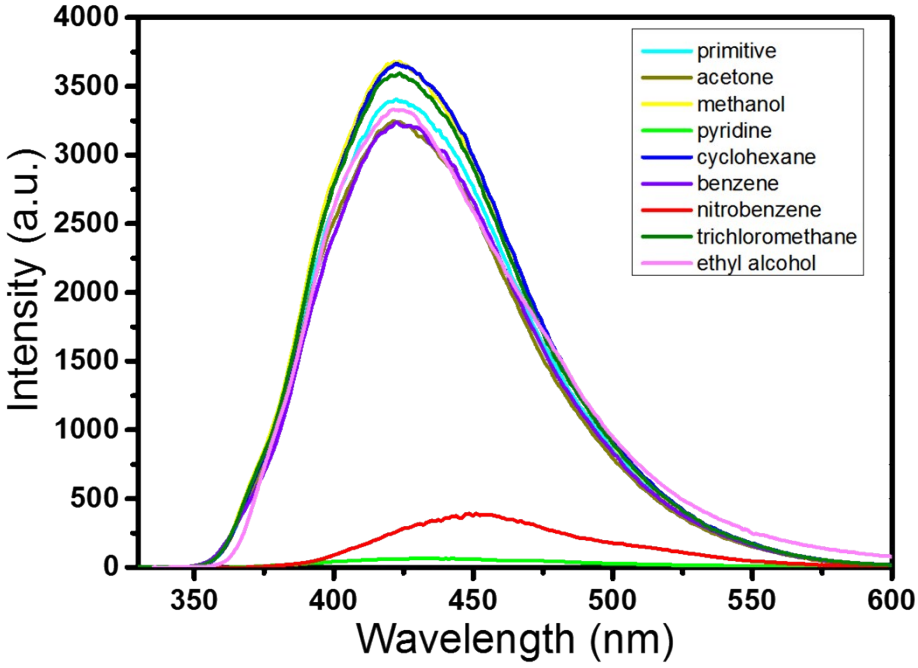

Figure S5. The phosphorescent response profiles of the (TA/LDHs@PAA)$_{80}$ TF to different VOCs.

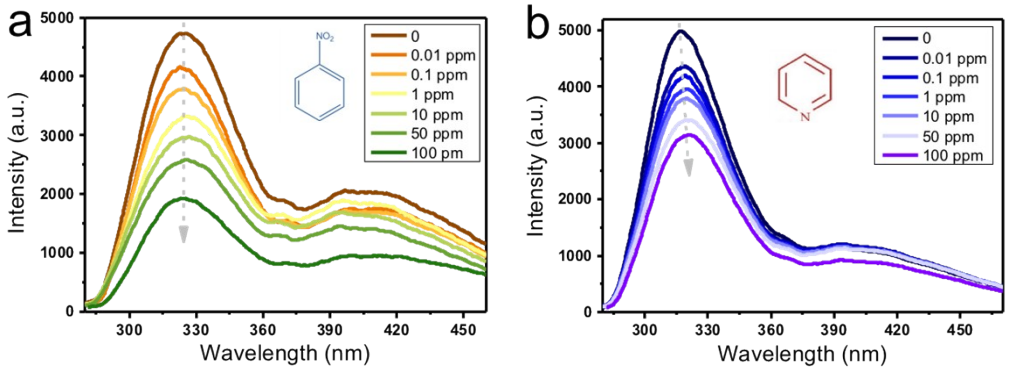

Figure S6. The fluorescent response profiles of the $(TA/LDHs@PAA)_{80}$ TF to (a) nitrobenzene and (b) pyridine with different concentrations.

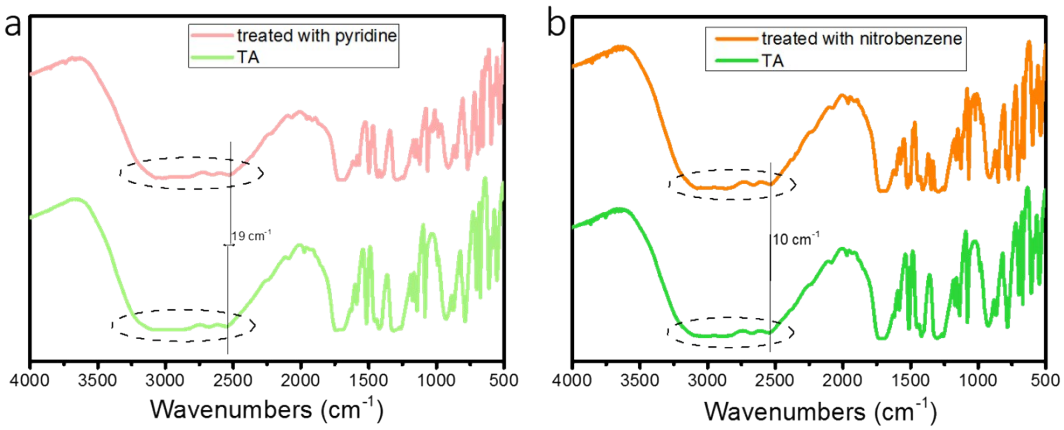

Figure S7. FT-IR spectra of the TA/LDHs@PAA before and after treated with (a) pyridine (b) nitrobenzene.